

# Observation of the pressure effect in simulations of droplets splashing on a dry surface.

A.M.P. Boelens,<sup>1</sup> A. Latka,<sup>2</sup> and J.J. de Pablo<sup>1</sup>

<sup>1</sup>*Institute for Molecular Engineering, University of Chicago,  
5801 South Ellis Avenue, Chicago, Illinois 60637, USA*

<sup>2</sup>*Department of Physics, University of Chicago, 5720 South Ellis Avenue, Chicago, IL 60637, USA*

(Dated: December 3, 2024)

At atmospheric pressure, a drop of ethanol impacting on a solid surface produces a splash. Reducing the ambient pressure below its atmospheric value suppresses this splash. The origin of this so-called pressure effect is not well understood and this is the first study to present an in-depth comparison between various theoretical models that aim to predict splashing and simulations. In this work the pressure effect is explored numerically by resolving the Navier-Stokes equations at a 3-nm resolution. In addition to reproducing numerous experimental observations, the simulations allow us to identify a previously unknown high-speed “rolling” contact line regime. Furthermore, the simulations reveal the existence of an early-time viscous length scale for lamella formation and a late time surface tension length scale. Our scaling analysis suggests that there is universal physics across different splashing regimes.

## I. INTRODUCTION

A wide variety of outcomes can occur when a liquid droplet hits a dry solid surface. Depending on impact velocity, surface tension, viscosity, ambient pressure, and surface roughness, one can observe deposition, splashing, receding breakup, or a rebound of the droplet [1]. The effect of ambient pressure on the transition between the smooth droplet-deposition and the splashing regimes is particularly intriguing. While intuition suggests that pressure should have a stabilizing effect, it has been found that lowering, instead of increasing the ambient pressure, suppresses splashing [2]. Despite various attempts to capture this so-called “pressure effect” in numerical simulations [3–5], its origins are still unknown. This knowledge gap has hindered technological developments, as there are numerous applications that could benefit from control over the splashing of droplets, including erosion, coating, cleaning, cooling, high-throughput drug screening, and fabrication techniques that rely on inkjet printing technology [6, 7].

One of the challenges associated with descriptions of the pressure effect is the multiscale nature of splashing. Length scales range from the contact line, where intermolecular forces act at nanometer length scales, to the characteristic length scale of the droplet itself, typically on the order of millimeters or larger. Time scales range from microseconds before impact, when deformation of the droplet leads to formation of the “central” air bubble [8–10], to milliseconds after impact when, as the liquid spreads radially in a thin film or lamella, the liquid sheet that was ejected from this lamella breaks up into many smaller droplets. While past efforts have tried to identify a single splashing criterion [11, 12], all these length and time scales must be resolved or modeled in order to fully capture the physics of splashing.

In this paper, by fully resolving the Navier-Stokes equations, we reproduce the pressure effect on splashing and, in doing so, reveal a number of features that help explain its origins. This is achieved by performing calculations with spatial and temporal resolutions as high as 3nm and 0.5ps. These are length and time scales which are currently inaccessible to experiments. To obtain such high resolution, the simulations of droplets splashing on a dry surface presented in this work are restricted to a two-dimensional axisymmetric geometry.

In addition to reproducing the pressure effect, the simulations describe several experimentally observed phenomena, including the formation of the central air bubble [8, 9], the formation and ejection of a liquid sheet [9, 13], the contact line-instability leading to entrainment of gas bubbles at the liquid/gas interface [14], and the scaling of the height of a very thin nm scale gas film under the droplet as function of impact velocity which is consistent with literature [10, 15]. Several intriguing new findings are also revealed by the simulations. First, we find that three-dimensional instabilities are not strictly necessary to reproduce the pressure effect. Second, we report the existence of two contact-line regimes: a new high-speed “rolling” contact-line regime, and a low-speed “sliding” contact-line regime. The observation of the “rolling” regime provides an explanation for the recent experimental discovery that splashing is independent of the wetting properties of the surface [16]. Third, a parameter sweep of lamella formation, varying impact velocity, viscosity, and surface tension, allows us to evaluate three recently proposed theories of splashing and lamella formation. One of these proposes air entrainment at the contact line, also known as dewetting [17], as well as the existence of a lift force [18], as the mechanisms responsible for liquid-sheet formation and breakup. Another theory attributes splashing to a “skating” motion of the droplet on a thin gas film, and the deflection of liquid on the impact surface [10]. The third theory [19] proposes that lamella formation is caused by the interaction of viscous and inertial length scales. All these theories show a different scaling of the lamella ejection velocity as function of impact velocity. While it is not possible to identify the correct scaling law from the currently available data, the theories

are not able to capture both the effect of surface tension and that of viscosity as predicted by full-blown numerical simulations. In addition, the dewetting assumption implies that splashing depends on the wetting properties of the surface [17], a hypothesis that is not consistent with our findings and experimental results [16]. Instead, we find that the early time scaling of the height of the lamella before ejection as function of time is the same for both splashing and simple droplet deposition, suggesting the existence of a universal theory. Additionally, we define a new lamella length scale for the surface tension. Pertaining to the breakup of the liquid sheet, our results support the concept of a lift force acting on the liquid sheet, which was proposed as part of the dewetting theory; however, they disagree with the idea suggested by the skating-droplet theory that it is the deflection of liquid on the solid surface that causes a drop to splash.

## II. THEORY & METHODS

To facilitate the tracking of topological changes, a Volume of Fluid approach [20] is adopted in this work. The VOF approach evolves around the definition of a phase parameter  $\alpha$  with the following properties:

$$\alpha = \begin{cases} 0 & \text{in gas phase} \\ (0, 1) & \text{on interface} \\ 1 & \text{in liquid phase} \end{cases} \quad (1)$$

The evolution of  $\alpha$  is calculated using the following transport equation:

$$\frac{\partial \alpha}{\partial t} + \nabla \cdot (\alpha \vec{v}) + \nabla \cdot (\alpha (1 - \alpha) \vec{v}_{lg}) = 0, \quad (2)$$

where  $\vec{v}$  is the phase averaged velocity, and  $\vec{v}_{lg}$  is the velocity difference between the liquid and the gas phase. This equation is equivalent to a material derivative, but rewritten to minimize numerical diffusion [21].

The phase parameter is used to calculate the phase averaged density,  $\rho$ , velocity,  $\vec{v}$ , and viscosity,  $\mu$ , which are used in the momentum balance:

$$\frac{\partial \rho \vec{v}}{\partial t} + \nabla \cdot (\rho \vec{v} \otimes \vec{v}) = -\nabla p + \nabla \cdot (\mu \nabla \vec{v}) + \rho \vec{g} - \vec{f}, \quad (3)$$

and the continuity equation:

$$\nabla \cdot \vec{v} = 0. \quad (4)$$

In the above equations  $t$  is time,  $p$  is pressure,  $g$  is gravity,  $\vec{f}$  is any body force, like the surface tension force, and  $\otimes$  is the dyadic product. To complete the VOF model, an expression is needed to calculate the surface tension force  $\vec{f}_{st}$ , and the initial and boundary conditions need to be chosen. The surface tension force is calculated using the expression [22]:

$$\vec{f}_{st} = \sigma_{st} \kappa \nabla \alpha \quad (5)$$

where  $\sigma_{st}$  is the surface tension coefficient, and  $\kappa$  is the curvature of the interface.

The computational domain has two different kinds of boundary conditions for each variable; on the bottom there is the impact wall, and on the sides and top there are boundary conditions which allow for the in and out flow of gas. As boundary condition for  $\alpha$  on the impact wall the Generalized Navier Boundary Condition is used [23, 24]. With this boundary condition the dynamic contact angle is allowed to vary freely, but a restoring line-tension force is applied at the contact line whenever the dynamic angle deviates from the equilibrium contact angle. This restoring force is an additional source term in the Navier-Stokes equations, and has the following form:

$$\vec{f}_{lt} = -\frac{\sigma_{st}}{h} \cos \theta_0 \nabla_{2D} \alpha \quad (6)$$

This force is applied on the liquid-gas interface in the first grid cells next to the wall and balances the surface tension force when the dynamic contact angle  $\theta$  is equal to  $\theta_0$ . In the above equation  $\sigma_{st}$  is the surface tension coefficient,  $h = V/A$ , is the mesh height, with  $A$  the surface area of the wall in a grid cell, and  $V$  its volume, and  $\nabla_{2D} \alpha$  is the gradient of  $\alpha$  on the wall. More information on the derivation and validation of this boundary condition can be found in Ref. [25]. On the wall the velocity obeys the Navier-slip boundary condition with a slip-length of  $\lambda_N = 1\text{nm}$ . For

mass conservation, the boundary condition for the pressure enforces both a zero flux and a zero second derivative of the pressure normal to the wall.

On the other sides of the simulation box the phase parameter,  $\alpha$ , obeys a Dirichlet fixed-value boundary condition for inflow and a zero-gradient Neumann boundary condition for outflow. The Dirichlet fixed value is set to zero, which is equivalent to only allowing gas to flow in. For each grid cell next to a side wall the local inflow velocity is calculated from the wall-face normal component of the velocity vector associated with the center of that specific grid cell. The boundary condition for the outflow velocity is a zero-gradient Neumann boundary condition. The total pressure  $p_0$  on the side walls is kept constant according to a simplified Bernoulli's equation:

$$p_0 = p + \frac{1}{2}\rho |\vec{v}|^2 . \quad (7)$$

In this boundary condition the gas is assumed inviscid, and when the gas inflow velocity,  $\vec{v}$ , changes, the pressure,  $p$ , changes accordingly. The above equations are solved using the VOF solver of the OpenFOAM Finite Volume toolbox [26].

The accurate description of the velocity and pressure fields upon impact requires that the deformation of the droplet be captured as it falls. To allow the droplet to equilibrate with the gas flow around it the droplet first falls through a large simulation box of  $1 \times 5$ mm at a relatively low resolution of  $320 \times 1600$  grid cells. Towards the wall, the mesh is refined six times. Each refinement divides a grid cell into four, giving a smallest grid size of 50nm. As initial condition for  $\alpha$ , the droplet is assumed to be a perfect sphere, with its center of mass located at a height of 4.5mm above the surface. To reach faster convergence of the gas velocity field, Stokes flow is assumed both inside and outside the droplet as initial condition, and stresses are matched on the interface [27]. The pressure field does not need to be initialized and develops as the simulation progresses. Once the droplet is sufficiently close to the wall, the simulation results in the lower part of the large simulation box are saved and re-initialized within a small box of  $1 \times 0.5$ mm with a resolution of  $320 \times 160$  grid cells which gets refined towards the wall. The results presented in this work are from simulations at two different refinement levels. To capture the details at the contact line and to capture splashing it is sufficient to refine the mesh eight times at the wall, for a minimum grid size of about 12nm. From a computational point of view, this is the smallest feasible mesh size that we can adopt for this system to run the simulations long enough to observe splashing. A second set of simulations focuses only on very early times. Because they run for a much shorter time it is possible to refine the mesh ten times and obtain an even higher resolution of about 3nm. Complete convergence at the contact line would require a grid size below the slip length, which is approximately 1nm and is beyond the reach of our computational resources. Nevertheless, at grid sizes of 3nm and 12nm the necessary physics of splashing are already present, and we expect the main observations of our simulations to be qualitatively correct. The width of both boxes is chosen to be large enough for the splash to occur within their confines.

For the simulations of a full splash the impact velocity is  $v_0 = 10.0\text{m s}^{-1}$  and the fluids are ethanol, for the liquid phase, and air, for the gas phase. This combination has been used in experiments [2], and has the advantage of showing an early splash, i.e. one that occurs shortly after impact. In experiments, the pressure effect is observed at moderately reduced gas pressures [2]. We therefore assume the dynamic viscosity of the air to be constant [28], but the density and the kinematic viscosity are allowed to change as pressure is reduced [28]. The reduced ambient pressure used in the simulations was deliberately chosen to be significantly lower than the experimentally observed threshold pressure, to ensure that the simulations were performed well into the suppressed splashing regime.

The impact velocities for the simulations resolving the early time scales are  $v_0 = 2.5\text{m s}^{-1}$ ,  $v_0 = 5.0\text{m s}^{-1}$ , and  $v_0 = 10.0\text{m s}^{-1}$ . The liquid viscosity is either the viscosity of ethanol or ten times that of ethanol and the surface tension is either the normal surface tension between air and ethanol or twenty times this surface tension, which is of the same order as the surface tension of mercury in air. In order to keep memory requirements within the constraints of our infrastructure, we consider a two-dimensional axisymmetric droplet with a diameter of  $300\mu\text{m}$  (as opposed to the 3mm droplets used in experiments [2]).

### III. RESULTS

#### A. Pressure effect and central air bubble

Figure 1 shows a time series of the pressure effect for a droplet approaching the surface at  $v_0 = 10\text{m s}^{-1}$ . The top half shows three images of droplet impact and liquid sheet ejection on a completely wetting surface at ambient pressure,  $p_0 = 100\text{kPa}$ . The first frame, Figure 1a, shows the droplet right after impact. As the droplet approaches the wall, gas pressure builds up at the stagnation point to about  $p = 1200\text{kPa}$ . This causes the droplet to deform, and an air pocket in the shape of a spherical dome appears underneath it. As the gap between the surface and the droplet closes, air gets squeezed out and reaches velocities of up to  $|\vec{v}| = 150\text{m s}^{-1}$ . When the liquid eventually touches the

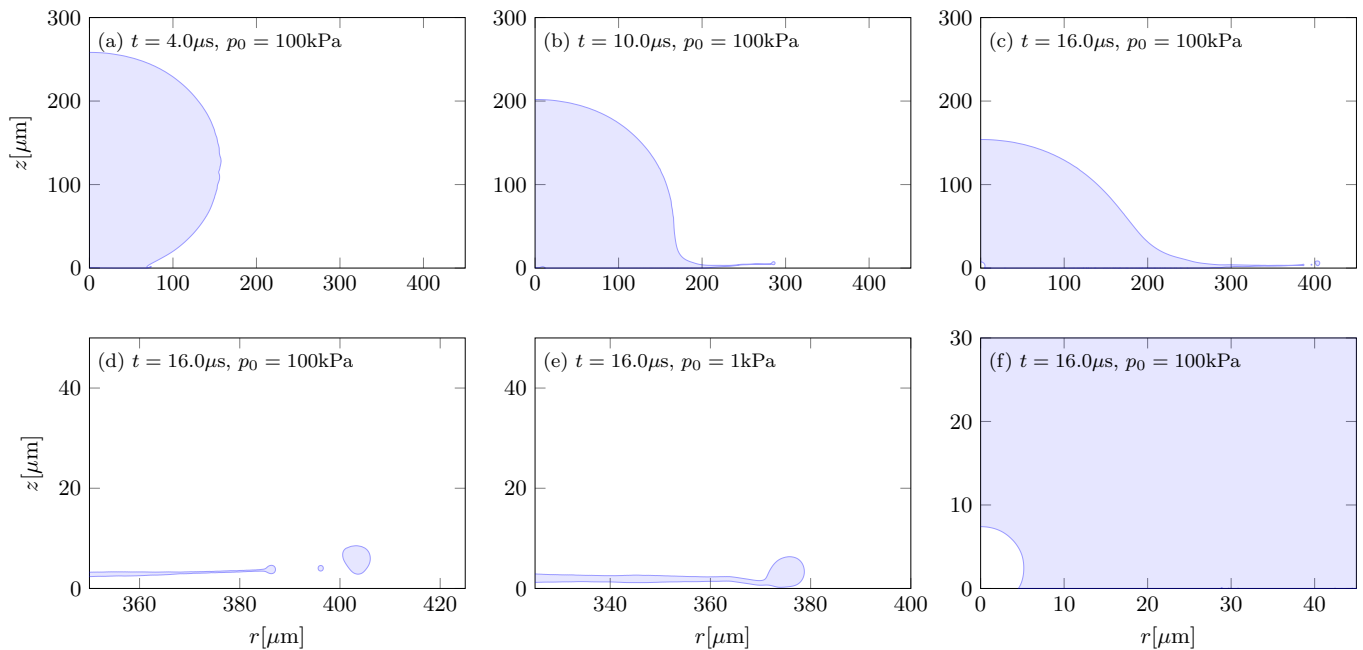


Figure 1. Time series of the impact of a droplet on a dry surface. The top frames (a-c) show simulation results for atmospheric pressure at different times. The bottom frames show (d) liquid sheet breakup at atmospheric pressure, (e) no breakup at reduced pressure, and (f) the central air bubble.

wall, a small amount of air is permanently trapped, forming the central air bubble with a diameter of about  $d = 10\mu\text{m}$  [8–10]. This bubble can be seen in Figure 1f.

Right after impact a liquid sheet is ejected with a velocity of approximately  $v_e = 100\text{m s}^{-1}$ . The liquid sheet forms at both atmospheric,  $p = 100\text{kPa}$ , and reduced pressure,  $p_0 = 1\text{kPa}$ . However, at atmospheric pressure the sheet gets lifted and breaks up into smaller droplets; in contrast, at reduced pressure it stays close to the surface and remains intact. Figure 1c shows the liquid sheet as it breaks up into smaller droplets at atmospheric pressure. Figure 1d shows a magnified image of the liquid sheet as it breaks up. The droplet that breaks off has a diameter of  $d = 7\mu\text{m}$ . Figure 1e shows a snapshot taken at the same time, but at a reduced pressure. One can see that instead of breaking up, the liquid sheet stays in one piece: splashing is suppressed by decreasing the ambient pressure. More detailed information on the thickness profiles of both the gas layer and the liquid sheet can be found in the Supporting Information.

The reproduction of the pressure effect in our simulations in itself leads to important conclusions. To reduce the number of variables, both the liquid and gas phases are assumed to be incompressible; this indicates that a shock wave cannot be solely responsible for liquid sheet formation [9]. Also, vortex formation in the gas phase upon impact is not necessary for splashing [29]. Although the vortices are not resolved in our simulations, the effect of pressure is still captured. Lastly, the break up of the liquid sheet is thought to be caused by either a Plateau-Rayleigh instability, or a Rayleigh-Taylor instability [30]. Although a Plateau-Rayleigh instability can play a role in three-dimensional splashing, since in these two-dimensional simulations breakup is still observed, it can be concluded that such an instability is not a necessary condition to observe splashing.

## B. Contact line instability

Perhaps the most useful aspect of our simulations is that they provide access to length and time scales that are not easily observed in experiments. This feature is illustrated in Figure 2, which presents a magnified time series of the liquid/gas interface at the contact line. A blue color corresponds to the liquid phase and white to the gas phase. These snapshots are taken at atmospheric pressure, from the moment just after impact until the point when the edge of the droplet is about to leave the simulation box. Drop impact is defined as the moment that an undeformed droplet would have hit the surface, at  $t = 6.2\mu\text{s}$ . Figure 2a shows the contact line just after impact and right before a liquid sheet forms at  $t = 6.33\mu\text{s}$ . Once the liquid sheet forms, which can be seen in Figure 2b, it is ejected right away. A feature revealed by experiments [9] is contact line dewetting. At high speeds the interface in front of the contact line becomes unstable and touches down on the surface, causing gas bubble entrainment at the contact line. This

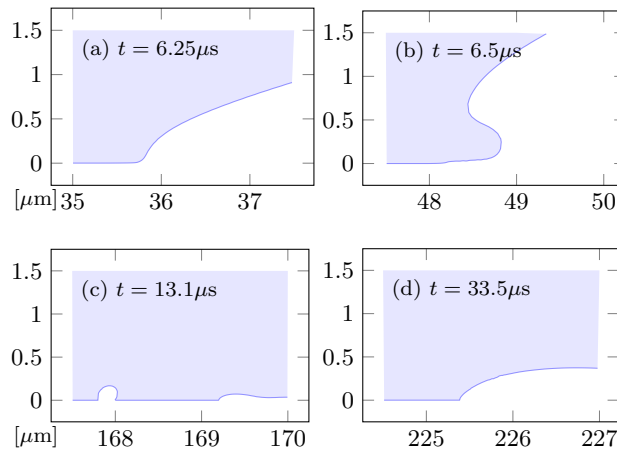


Figure 2. Time series of the droplet interface showing the evolution of the contact line at atmospheric pressure. Light blue represents the liquid phase. The vertical axis shows the distance normal to the surface and the horizontal axis shows the distance parallel to the surface relative to the center of the droplet. Both axes are in  $\mu\text{m}$ .

phenomenon can be appreciated in Figure 2c, which at  $r \approx 168\mu\text{m}$  shows a gas bubble that formed when the contact line became unstable, and the liquid in front of the contact line touched down on the surface. The first touch-down event is observed at  $t = 7.33\mu\text{s}$ , and at  $t = 14.4\mu\text{s}$  the contact line stabilizes again. Figures 2c and 2d are well within the unstable and stable contact-line regimes, respectively.

### C. Gas film dynamics

While the pressure effect, the central air bubble, and contact line instabilities are all reproduced, because the droplets in the simulations are significantly smaller than the droplets used in experiments a direct comparison is not straightforward. However, it is possible to compare the scaling laws reported in the literature with the results of simulations. As mentioned in the introduction, one of the theories for splashing predicts the existence of a very thin gas film under the droplet [10]. This gas film is shown in figure 3 for different impact velocities and different properties of the liquid. The vertical axis shows the distance from the wall and the horizontal axis the radial distance away from the center of the droplet. Both axes are in  $\mu\text{m}$ . The figures on the left ((a), (c), and (e)) correspond to an impact velocity of  $0.25\text{m s}^{-1}$  and the time difference between successive lines is  $1.0\mu\text{m}$ . The figures on the right ((b), (d), and (f)) show an impact velocity of  $10.0\text{m s}^{-1}$ , and the time difference between successive lines is  $0.1\mu\text{m}$ . The top figures ((a) and (b)) show the results for ethanol, the middle figures ((c) and (d)) show the results for the high viscosity liquid, and the bottom figures ((e) and (f)) show the results for the liquid with a high surface tension. Comparing figure (a) and (c), shows that a higher viscosity results in a thicker gas film. Comparing figures (a) and (b) shows that a higher impact velocity gives a thinner gas film. Both findings are consistent with literature [15]. An increase in surface tension also gives an increased gas film thickness.

A more quantitative representation of the gas film height can be seen in figure 4. This figure shows the height of the gas film at the edge of the droplet at the moment of lamella formation as a function of impact velocity. While the pre-factor is different due to differences in geometry, the scaling is consistent with theory [10]. The thin gas film has also been observed in recent experiments, both directly [31] and indirectly [32].

While the observations of the central air bubble, contact line instability, and pressure effect connect our results qualitatively with the existing literature, the scaling of the height of the gas film as function of impact velocity shows that our results are also in quantitative agreement with experiment, serving to validate key aspects of the model. Our results also suggest that the existence of a gas film is essential for a droplet to be able to splash; in fact, when the simulations are run at a coarser resolution, at which the lamella is fully resolved but the gas film is not, the lamella sticks to the surface and there is no splash, even at high gas pressures.

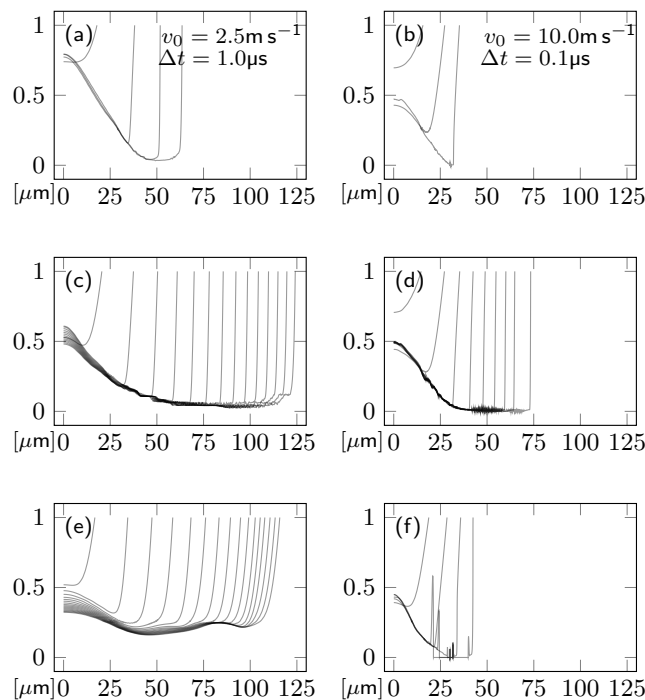


Figure 3. Gas film profiles of different droplets approaching the wall. The vertical axis shows the height above the wall and the horizontal axis the radial distance away from the center. Both axes are in  $\mu\text{m}$ . The figures on the left ((a), (c), and (e)) show an impact velocity of  $0.25\text{m s}^{-1}$  and the time difference between successive lines is  $1.0\mu\text{s}$ . The figures on the right ((b), (d), and (f)) show an impact velocity of  $10.0\text{m s}^{-1}$  with a time difference of  $0.1\mu\text{s}$ . The top figures ((a) and (b)) show the results for ethanol, the middle figures ((c) and (d)) show the results for the high viscosity liquid, and the bottom figures ((e) and (f)) show the results for the liquid with a high surface tension. Comparing figure (a) and (c), consistent with literature [15], a higher viscosity results in a thicker gas film. Comparing figures (a) and (b), a higher impact velocity gives a thinner gas film. An increases surface tension also gives an increased gas film thickness.

#### D. Air film thickness

Considering the thickness of the gas film under the droplet upon impact and the thickness of the gas film under the liquid sheet after ejection, it would be a valid question to ask whether the continuity assumption is valid in these simulations and how a breakdown of the continuity assumption would affect the simulation results.

For the gas film present under the droplet upon impact, Mandre and Brenner [10] show that at larger impact velocities the continuum assumption breaks down and they predict that this leads to earlier rupture of the gas film. As a droplet spreads over a surface, the gas film under the droplet continuously grows at the contact line. Because the gas film was most recently formed at the contact line, this is where breakdown of the gas film is least likely to happen. Therefore the earlier rupture of the gas film due to the breakdown of the continuum assumption will most likely not affect lamella formation, and the simulation results are expected to remain valid.

To be able to analyze the thickness of the gas film under the liquid sheet, Fig. 5 shows a time series of the contour of the droplet at atmospheric pressure with the vertical axis plotted on a logarithmic scale. Since the vertical axis cannot go to zero, it is cut off at  $10^{-3}\mu\text{m}$ , and the center of the drop corresponds to the vertical axis. Fig. 5a shows the droplet right after impact with the central air dome clearly visible. Initially the bubble is slightly under  $1\mu\text{m}$  high, and about  $30\mu\text{m}$  wide. The vertical lines or peaks under the droplet are small air bubbles which were trapped on impact. The next figure shows the droplet right after a liquid sheet is ejected and the third frame shows the droplet in the unstable contact line regime. The vertical lines behind the contact line are small air bubbles which were entrained by the moving contact line. Also, it can be observed how the contact line of the central air bubble is moving toward the center. The gas layer under the liquid sheet is on the order of several microns thick. The last figure, Fig. 5d, shows the droplet with a stable contact line. There are no longer droplets being trapped right behind the contact line. Instead, there is just one cavity present at the contact line with a height of a little under  $1\mu\text{m}$ . The gas film right after the cavity has a thickness of about  $0.1\mu\text{m}$ , and increases again to several microns towards the rim of the liquid sheet.

To put the above numbers in perspective they need to be compared to the mean free path of air. At room

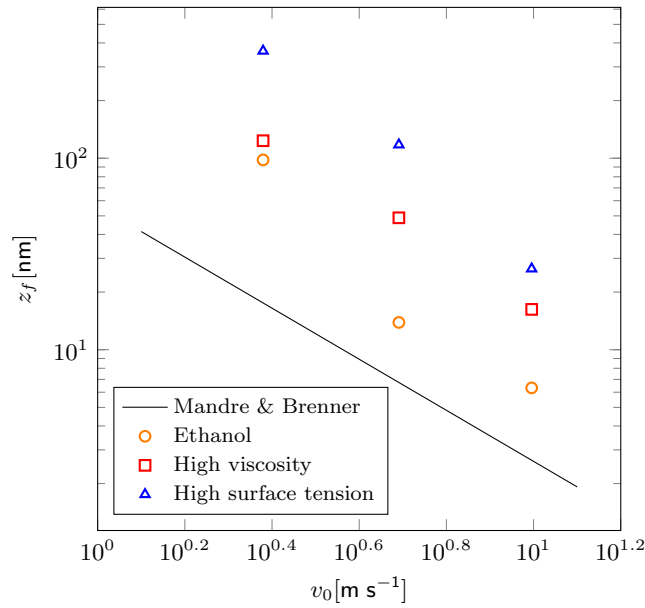


Figure 4. Height of the gas film under the drop at the moment of lamella formation for various velocities, viscosities, and surface tensions. The line shows the theoretical predictions by Mandre and Brenner [10],  $z_f \approx 60r_0\text{St}^{4/3}$ , with  $\text{St} = \mu_g/(\rho_l v_0 r_0)$ .  $r_0$  is the radius of the droplet,  $\rho_l$  is the liquid density, and  $\mu_g$  is the gas viscosity.

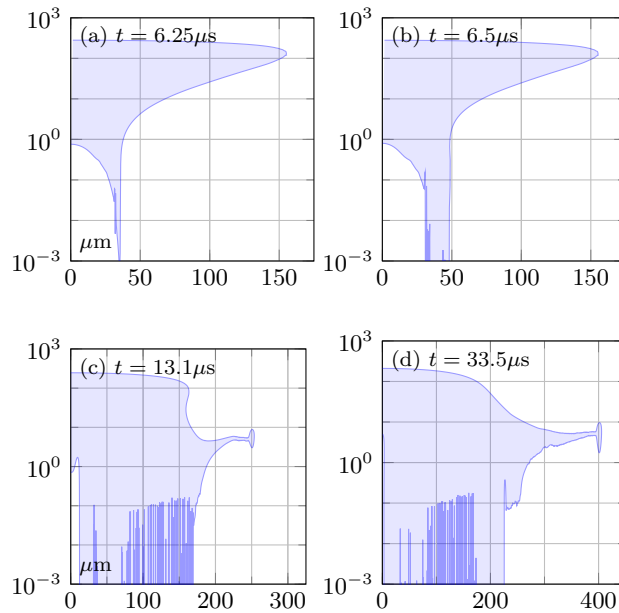


Figure 5. Time series of the droplet interface with the vertical axis plotted on a logarithmic scale. The axis are in  $\mu\text{m}$ .

temperature and atmospheric pressure the mean free path is around  $\lambda \approx 70\text{nm}$  [33]. The typical thickness of the gas layer is several microns, so the continuity approximation should be valid for these simulations. Since the mean free path scales with the kinematic viscosity, at the reduced pressure the mean free path is about  $\lambda \approx 7\mu\text{m}$ , which is about the same height as the typical thickness of the gas layer. This means that at reduced pressure the validity of the continuum approximation is pushed to its limits, and that the simulations may slightly overestimate the longevity of the gas film under the liquid sheet at reduced pressure. However, as long as liquid sheet was ejected fast enough, the gas film would break down far behind the rim of the liquid sheet and this would not affect the simulation results.

### E. Rolling contact line regime

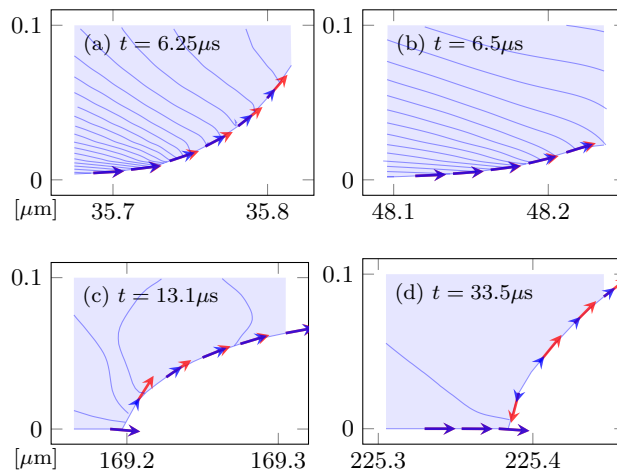


Figure 6. Time series of the droplet interface, and non-dimensional interface velocity,  $\hat{v}_i$ , showing the evolution of the contact line at atmospheric pressure. This time series is magnified 15 times compared to Figure 2. The unit vector is shown as ( $\rightarrow$ ), and the non-dimensional interface velocity as ( $\rightarrow$ ). Light blue represents the liquid phase, and the axes are in  $\mu\text{m}$ . The contour lines are iso-velocity lines,  $|v|$ , and the difference between each line is  $2.5\text{m s}^{-1}$ .

An important consequence of the existence of a thin gas film under the droplet can be seen in Figure 6. In this figure a magnified time series of the contact line and non-dimensional interface velocity,  $\hat{v}_i$ , is shown at atmospheric pressure. While in the last two frames a normal low-speed contact line can be observed, the first two frames show a strongly curved interface, which continues under the droplet. To gain more insight into the behavior of the curved interface at the contact line, we now focus on the non-dimensional interface velocity,  $\hat{v}_i$ . To calculate the non-dimensional interface velocity, the velocity of the interface,  $\vec{v}_i$ , is decomposed into a component tangential to the interface,  $\vec{v}_{i,t}$ , and a component in the direction of the translation of the interface,  $\vec{v}_{i,r}$ . The tangential velocity is then made non-dimensional according to:  $\hat{v}_i = \vec{v}_{i,t} / |\vec{v}_{i,r}|$ . When an object is undergoing a purely “rolling” motion, e.g. a cylinder rolling over a surface, the magnitude of the tangential component of the interface velocity is equal to the magnitude of the translational component, and the magnitude of the non-dimensional interface velocity is unity. When the tangential and translational velocities are not equal, and the object is (partly) slipping, the non-dimensional interface velocity is no longer unity. When comparing the non-dimensional interface velocity vector field with the unit vector field, it can be observed that at early times the non-dimensional interface velocity is very close to one, and thus the interface rolls over the surface at a high speed, like a caterpillar track. At later times, the non-dimensional interface velocity is much smaller than unity, indicating that, at low velocities, contact line movement is dominated by slip. In addition to the non-dimensional interface velocity, the figures also show contour lines of the magnitude of the velocity in increments of  $v = 2.5\text{m s}^{-1}$ . It can be appreciated that in the first two frames the contour lines close to the wall run nearly parallel to the interface, providing further support for a rolling contact line. The introduction of a rolling contact line also provides a possible explanation for the recent experimental finding that splashing is independent of the wetting properties of the surface [16]. When the contact line is in the rolling regime its contact angle is always 180 degrees, and thus it should behave in exactly the same manner on wetting and non-wetting surfaces. Therefore, in this regime, liquid-sheet formation is predicted to be independent of the wetting properties of the surface, a feature that is not consistent with the dewetting assumption for splashing [18].

### F. Lamella ejection

We now further examine the dewetting model [18], the skating-drop model [10], and the lamella-formation model [19] by investigating their predicted lamella ejection velocities as a function of the impact velocity for various liquid properties. The correct prediction of the ejection velocity is very important, because it determines whether a liquid sheet that breaks up at a later time will form or not [18]. For this analysis the relevant non-dimensional numbers of



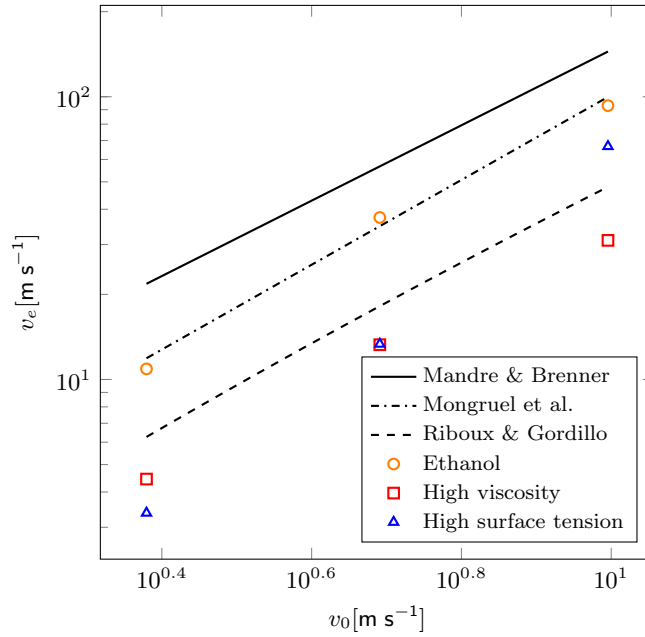


Figure 7. Lamella ejection velocity as function of the impact velocity of a droplet for various velocities, viscosities, and surface tensions. Ethanol refers to the simulations of ethanol in air, “High viscosity” refers to simulations of a fluid with 10 times the viscosity of ethanol in air, and “High surface tension” refers to simulations of a fluid with 20 times the surface tension of ethanol in air. The lines show theoretical predictions by Mandre and Brenner [10] ( $v_e \propto v_0^{4/3}$ ), Riboux and Gordillo [18] ( $v_e \propto v_0^{1.3}$  in current regime), and Mongruel *et al.* [19] ( $v_e \propto v_0^{3/2}$ ). The error bars in this figure are smaller than the symbols.

the system are:

$$\begin{aligned} \text{St} &= \frac{\mu_g}{\rho_l v_0 r_0}, & \text{We} &= \frac{\rho_l v_0^2 r_0}{\sigma}, \\ \text{Re} &= \frac{\rho_l v_0 r_0}{\mu_l}, & \text{Oh} &= \frac{\sqrt{\text{We}}}{\text{Re}}, \end{aligned} \quad \text{and}$$

where  $\text{St}$  is the inverse Stokes number,  $\text{Re}$  is the Reynolds number,  $\text{We}$  is the Weber number, and  $\text{Oh}$  is the Ohnesorge number. These numbers have the values:  $\text{St} = 1.3 \times 10^{-5}$ ,  $\text{We} = 528$ ,  $\text{Re} = 986$ , and  $\text{Oh} = 2.33 \times 10^{-2}$ , which were calculated using the following parameters:  $v_0 = 10 \text{ m s}^{-1}$ ,  $\rho_l = 789 \text{ kg m}^{-3}$ ,  $\mu_l = 1.20 \times 10^{-3} \text{ Pa s}$ ,  $\rho_g = 0.01 \text{ kg m}^{-3}$  at  $p_0 = 1 \text{ kPa}$ ,  $\rho_g = 1.00 \text{ kg m}^{-3}$  at  $p_0 = 100 \text{ kPa}$ ,  $\mu_g = 1.48 \times 10^{-5} \text{ Pa s}$ ,  $\sigma = 0.02239 \text{ J m}^{-2}$ , and  $r_0 = 150 \mu\text{m}$ . These numbers suggest that in our simulations impact is dominated by the inertia of the fluid.

Mandre and Brenner [10] calculate the non-dimensional liquid sheet ejection velocity with the following equation:

$$v_{e,M} = 0.34 \text{St}^{-1/3} \quad (8)$$

where the liquid sheet ejection velocity,  $v_{e,M}$ , is non-dimensionalized with the impact velocity,  $v_0$ . Riboux and Gordillo [18], on the other hand, calculate the ejection velocity with:

$$v_{e,R} = \frac{\sqrt{3}}{2} t_{e,R}^{-1/2}. \quad (9)$$

Where  $t_{e,R}$  is the sheet ejection time, non-dimensionalized with the impact velocity,  $v_0$ , and the droplet radius,  $r_0$ . To determine the sheet ejection time, the following equation is used:

$$c_1 \text{Re}^{-1} t_{e,R}^{-1/2} + \text{Re}^{-2} \text{Oh}^{-2} = c^2 t_{e,R}^{3/2} \quad (10)$$

Here  $c_1$  and  $c$  are two constants with the values  $c_1 = \sqrt{3}/2$  and  $c = 1.1$ . Lastly, Mongruel *et al.* [19] propose the following scaling for the non-dimensional ejection velocity:

$$v_{e,N} \propto \sqrt{\text{Re}} \quad (11)$$

The above equations give the results shown in Fig. 7. In this figure Ethanol refers to the simulations of ethanol in air, “High viscosity” refers to simulations of a fluid with 10 times the viscosity of ethanol in air, and “High surface tension” refers to simulations of a fluid with 20 times the surface tension of ethanol in air. The theoretical curves correspond to the predictions for ethanol drops in air. To plot the theoretical curves of Mandre and Brenner [10] and Riboux and Gordillo [18], the prefactors that are provided with their respective theories are used. Since, Mongruel *et al.* [19] do not provide a pre-factor, a prefactor of 0.275 was chosen to match the data. To be able to clearly observe the differences in scaling of the liquid sheet ejection velocity as function of the impact velocity, velocities are not non-dimensionalized.

At the outset, we hasten to note that the results from our simulations cannot distinguish unequivocally between the different proposed scaling laws for the lamella ejection velocity as function of the impact velocity. However, it is clear that the prefactors given by Mandre and Brenner [10] and Riboux and Gordillo [18] do not fit our data well. In the case of the skating-drop model, this could be attributed to differences in geometry. Their predictions are for droplets in a planar geometry, while the simulations were performed in an axisymmetric geometry. In the case of the dewetting model, this could be explained by the fact that the experiments that were used to fit their model did not have access to the time and length scales that these simulations can capture. Since the velocity of a lamella changes rapidly after ejection, this can lead to a significant error. The simulations also reveal other discrepancies. First, they show that lamella ejection velocity depends on surface tension and viscosity; the skating-drop model, however, does not incorporate either of these variables. The lamella formation model, on the other hand, does predict that the ejection velocities for high viscosity droplets are about  $\sqrt{10}$  times lower than the ejection velocities for the normal ethanol droplets. However, this model does not incorporate surface tension. Lastly, for the dewetting model, after fitting the model to our simulation data, we find that it correctly predicts the effect of surface tension, but not that of viscosity.

To further explore the effect of viscosity and surface tension, in Figure 8 we examine the early stages of lamella formation. Figure 8a shows the interface of a droplet depositing on the surface with a velocity of  $v_0 = 2.5\text{m s}^{-1}$  and a viscosity of ten times that of ethanol. Between every snapshot of the interface is a time difference of  $\Delta t = 2\mu\text{s}$ . Right after impact, a radial velocity maximum (yellow dots) can be observed on the interface; when we track the time evolution of this maximum, eventually a lamella forms at the location of the velocity maximum. After the lamella forms, when the radial position of the interface is plotted ( $r$ , as function of the height,  $z$ ), a neck or cusp appears that reflects a minimum of the interface (red dots), and the lamella, which represents a maximum of the interface (blue dots).

Figure 8b shows the radial position of these points as a function of time. The scaling with  $r \propto t^{1/2}$  is a theoretical prediction based on geometrical arguments and indicates that the radial positions of the velocity maximum and lamella are dominated by inertia. This is consistent with the literature [19]. Figure 8c shows the vertical positions of the data points as a function of time. We also show the scaling associated with viscosity,  $z_\nu \propto \sqrt{\nu t}$ , and inertia,  $z_I \propto v_0 t$ , as proposed by Mongruel *et al.* [19]. As can be appreciated in Figure 9, the scaling with  $t^{3/2}$  introduces a new length scale that is associated with surface tension.

Figure 9 further explores the evolution of the velocity maximum (i.e. the yellow dots in Figure 8) for various simulations. In Figure 9a the results are shown for droplets with a viscosity ten times that of ethanol at three different impact velocities. Non-dimensionalizing both the vertical position and time with the kinematic viscosity,  $\nu$ , and impact velocity,  $v_0$ , leads to a collapse of the data at early times. This confirms that at early times lamella formation is dominated by viscosity, as was predicted by Mongruel *et al.* [19]. Figure 9b shows the results of a droplet with a surface tension of twenty times that of ethanol impacting at three different velocities. This time the axis is scaled using surface tension,  $\sigma$ , liquid density,  $\rho$ , impact velocity,  $v_0$ , and diameter  $D$ . Again this leads to collapse of the data, suggesting that, for these droplets, late-stage lamella formation is dominated by surface tension. The height of the lamella scales as:  $z_\sigma \propto \sqrt{\sigma v_0 / (\rho D^2)} t^{3/2}$ . The fact that the same scaling of the lamella height before ejection as function of time can be observed for different material properties in Figure 7, and for different velocities in Figure 8 and Figure 9, suggests that a universal mechanism exists that causes the lamella to be created for splashing and depositing droplets. Capturing these different regimes could become a pre-requisite for emerging splashing theories, as opposed to a focus on low-viscosity splashes [10, 18].

## G. Liquid sheet velocity

In order to arrive at a criterion for whether a droplet will splash or not, a parameter  $\beta = v_{h_t,z} / v_{tc}$  can be defined [18], where  $v_{h_t,z}$  is the vertical velocity of the liquid sheet when it has risen to a characteristic height of  $h_t$ , and  $v_{tc}$  is the Taylor-Culick velocity. The parameter  $\beta$  describes whether a thin sheet gets lifted up, causing a drop to splash, or whether it re-wets the surface. In this work two different methods to calculate  $\beta$  are used; based on material properties and impact conditions, Riboux and Gordillo [18] provide a theoretical prediction for the value of  $v_{h_t,z}$ .

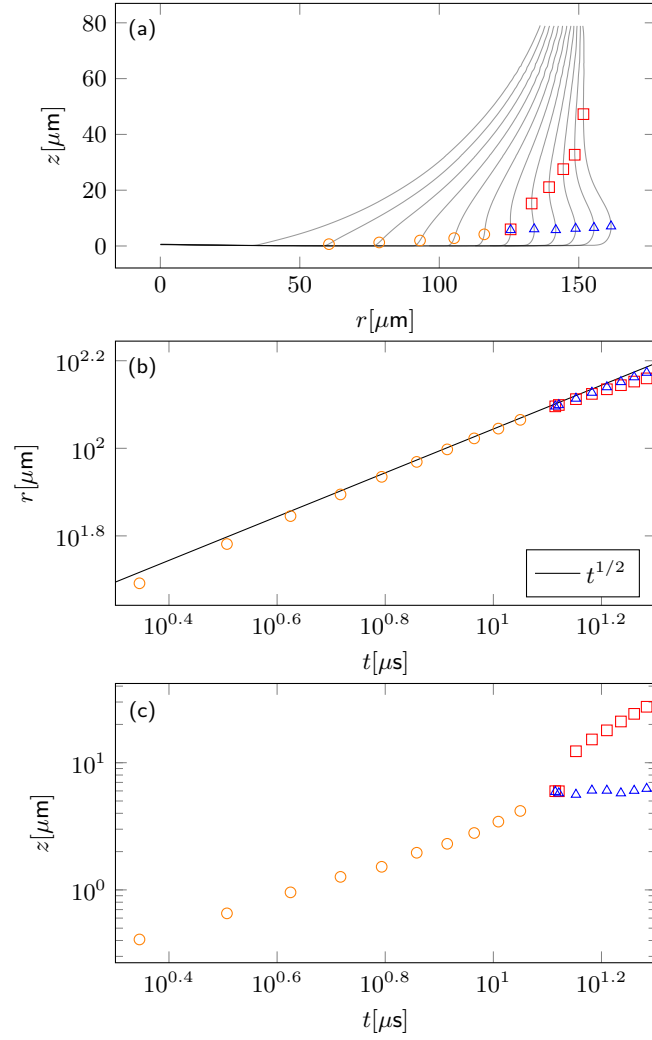


Figure 8. a) Interface evolution of droplet impact at  $2.5\text{ms}^{-1}$  with a liquid viscosity 10 times that of ethanol. A maximum in the horizontal velocity (  $\circ$  ) can be observed on the interface early after impact and can be traced to the time of lamella formation. At the moment of lamella formation there is a bifurcation for points following the cusp (  $\square$  ) and the lamella (  $\triangle$  ). b) The radial position plotted as function of time for the same data points as in Figure (a). The  $t^{1/2}$  scaling suggests that the flow is dominated by inertia. c) The vertical position of the velocity maximum, lamella and cusp as function of time.

When this theoretical value is used,  $\beta$  is called  $\beta_R$  and it is calculated using the equation:

$$\beta_R = \left( \frac{K_l \mu_g (v_{e,R} v_0) + K_u \rho_g (v_{e,R} v_0)^2 (h_t r_0)}{2\sigma} \right)^{1/2} \quad (12)$$

with:

$$K_l = -\frac{6}{\tan^2(\alpha)} \left[ \ln\left(16 \frac{l_g}{h_t r_0}\right) - \ln\left(1 + 16 \frac{l_g}{h_t r_0}\right) \right], \quad (13)$$

and:

$$K_u = 0.3. \quad (14)$$

In the above equation  $\alpha = 20/180 \pi^\circ$ , and  $l_g = 1.2\lambda$ , the slip length of the gas.  $\lambda = \lambda_0(p_{\text{atm}}/p_0)$  with  $\lambda_0 = 65\text{nm}$  the mean free path of air at room temperature and atmospheric pressure,  $p_{\text{atm}} = 100\text{kPa}$ . However,  $v_{h_t,z}$  can also be directly determined from the simulation data, in which case  $\beta$  is called  $\beta_S$  and is calculated from our simulations

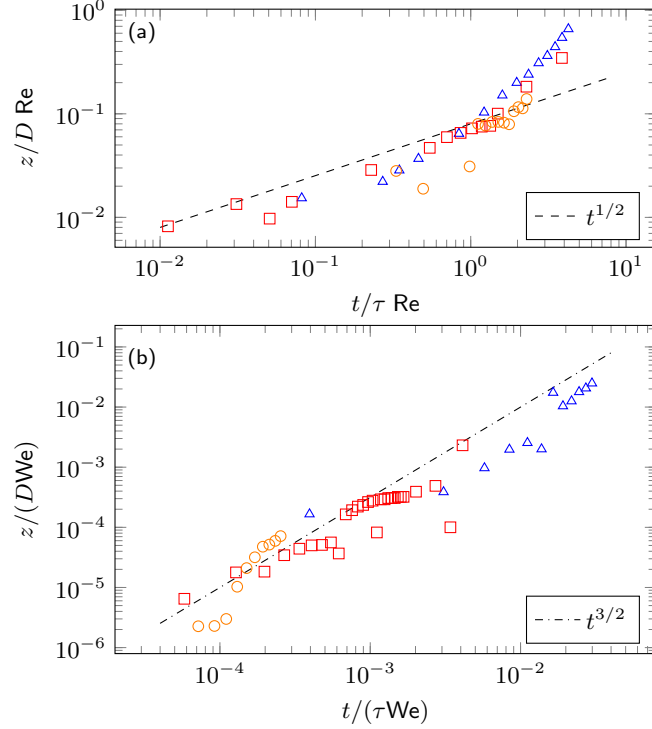


Figure 9. a) Non-dimensional vertical position of the velocity maximum as function of non-dimensional time for  $2.5\text{m s}^{-1}$  ( $\triangle$ ),  $5.0\text{m s}^{-1}$  ( $\square$ ), and  $10.0\text{m s}^{-1}$  ( $\circ$ ). The surface tension is that of ethanol and the viscosity is 10 times that of ethanol. The scaling suggests that at early times, lamella formation is dominated by viscosity. b) Non-dimensional vertical position of the velocity maximum as function of non-dimensional time for  $2.5\text{m s}^{-1}$  ( $\triangle$ ),  $5.0\text{m s}^{-1}$  ( $\square$ ), and  $10.0\text{m s}^{-1}$  ( $\circ$ ). The viscosity is the viscosity of ethanol and the surface tension is 20 times that of ethanol. The scaling suggests that at late times, the scaling for these droplets is dominated by surface tension.

using:

$$\beta_S = \frac{v_{h_t,z} v_0}{\sqrt{2\sigma/(\rho_l h_t r_0)}} \quad (15)$$

where  $v_{h_t,z}$  is the vertical velocity of the liquid sheet when it has risen a characteristic height of:

$$h_t = \frac{\sqrt{12}}{\pi} t_{e,R}^{3/2} \quad (16)$$

For  $p_0 = 1\text{kPa}$  this is the vertical velocity at  $t = 0.17$ , and for  $p_0 = 100\text{kPa}$  at  $t = 0.26$ . In Table I the theoretical

Table I. Comparison of simulation results with predictions of the model by Riboux and Gordillo [18] for two different ambient pressures. The table shows the ejection velocities, and the splashing criterion of the liquid sheet.  $v_e$ , and  $\beta_S$  are simulation results.  $v_{e,R}$ , and  $\beta_R$  are the predictions by Riboux and Gordillo

$\mathbf{P}_0[\text{kPa}]$	$\mathbf{v}_{e,R}$	$\mathbf{v}_e$	$\beta_R$	$\beta_S$
1	4.87	7.05	0.075	0.523
100	4.87	7.65	0.649	0.557

predictions of Riboux and Gordillo [18] are shown. The theoretically predicted values for  $\beta$  are  $\beta_R = 0.075$  and  $\beta_R = 0.649$  for calculations at  $p_0 = 1\text{kPa}$  and  $p_0 = 100\text{kPa}$ , respectively. However, the values calculated from the simulations are  $\beta_S = 0.523$  and  $\beta_S = 0.557$ . Comparing  $\beta_S$  and  $\beta_R$ , shows that theory predicts about an order of magnitude difference between the normal and reduced pressure cases. However, the values calculated from the simulations show similar values of  $\beta$  for both normal and reduced pressures. This suggests that when using the definition in equation 15,  $\beta$  is not able to predict splashing for these simulations.

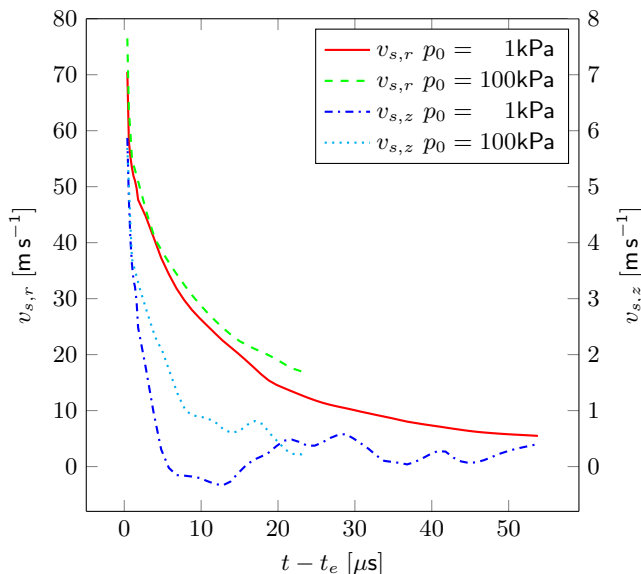


Figure 10. The radial and vertical velocity of the liquid sheets ejected from the droplet as function of time.  $t_e$  is defined as the moment of sheet ejection.

In addition to the parameter  $\beta$ , the simulations can also provide insight on how the velocity of the lamella evolves once, after formation, it gets lifted up and turns into a liquid sheet. This is shown in Fig. 10. In this graph,  $t = 0$  is the moment of liquid sheet ejection,  $t_e$ , which is defined as the moment a local maximum can first be detected in the width of the droplet close to the wall. This local maximum is the beginning of a liquid sheet. While in these calculations the value of  $\beta$  does not seem to represent a good criterion for splashing, the vertical velocity components, shown in Fig. 10, do suggest that a lift force could be responsible for the breakup of a liquid sheet. If liquid sheet breakup was determined at the time of liquid sheet ejection, i.e. the hypothesis of liquid deflecting on the surface that is suggested by the skating drop theory [10], one would expect very different vertical ejection velocities for both splashing and non-splashing droplets. However, initial vertical ejection velocities are very similar between the normal and reduced pressure cases. Only at later times, when a lift force could have started to act on the liquid sheet, do the velocities start to differ, supporting the lift force hypothesis. A possible explanation for the mismatch between the simulations and theory is that the experiments that were used to benchmark the fitting parameters in the theory could not have measured liquid sheet velocities at the early times observed in our simulations. In addition to supporting the lift force hypothesis, these simulations support the idea that splashing consists of multiple stages. A sheet must form first, which then gets broken up or not depending on physical parameters.

#### IV. CONCLUSIONS

In summary, high-resolution numerical simulations of splashing ethanol droplets appear to describe the so-called “pressure effect” with considerable fidelity. The formation of the experimentally observed central air bubble, air bubble entrainment at the contact line, liquid sheet formation, and the scaling of the height of the gas film under the droplet with impact velocity are all reproduced. Simulations have also allowed us to identify two distinct contact line regimes, at high and low liquid velocities. At high velocities, the contact line moves in a rolling fashion, while at low speeds the contact line slips on the surface, thereby providing an explanation for the experimental finding that splashing is independent of the wetting properties of the surface [16]. In addition, it is found that three-dimensional fluid instabilities are not needed to observe the pressure effect. The results of simulations do not allow us to distinguish between recently proposed scaling relations for the lamella ejection velocity as a function of the impact velocity (as described in [10], the dewetting theory [18], and the lamella formation theory [19]). However, the simulations do reveal that these models do not correctly capture the effect of both viscosity and surface tension. In particular, analysis of lamella formation at early times confirms that there is an early viscosity-dominated regime as predicted by Mongruel *et al.* [19]. In addition, it is possible to define a new length scale for the height of the lamella before ejection to describe the effect of surface tension. For the vertical acceleration of the liquid sheet and its subsequent breakup, the  $\beta$  parameter defined by Riboux and Gordillo does not appear to predict our numerical results, but support the

idea of liquid sheet acceleration by a lift force. Droplet deflection on the surface does not seem to be able to predict splashing.

## ACKNOWLEDGMENTS

The authors would like to thank Sidney R. Nagel, Michelle Driscoll, and Casey Stevens, for many fruitful discussions of the simulation results.

- 
- [1] A. L. Yarin, “Drop impact dynamics: splashing, spreading, receding, bouncing. . .,” *Annu. Rev. Fluid Mech.* **38**, 159–192 (2006).
  - [2] Lei Xu, Wendy W Zhang, and Sidney R Nagel, “Drop splashing on a dry smooth surface,” *Physical review letters* **94**, 184505 (2005).
  - [3] Laurent Duchemin and Christophe Josserand, “Curvature singularity and film-skating during drop impact,” *Physics of Fluids (1994-present)* **23**, 091701 (2011).
  - [4] Go Taura and Mitsuhiro Matsumoto, “Molecular Dynamics Simulation of Microdroplet Impingement on Solid Surface,” *Journal of Fluid Science and Technology* **5**, 207–218 (2010).
  - [5] Joel Koplik and Rui Zhang, “Nanodrop impact on solid surfaces,” *Physics of Fluids (1994-present)* **25**, 022003 (2013).
  - [6] C Josserand and ST Thoroddsen, “Drop impact on a solid surface,” *Annual Review of Fluid Mechanics* **48**, 365–391 (2016).
  - [7] A. K. Price, A. B. MacConnell, and B. M. Paegel, “Microfluidic bead suspension hopper,” *Anal. Chem.* **86**, 5039–5044 (2014).
  - [8] S Chandra and CT Avedisian, “On the collision of a droplet with a solid surface,” *Proceedings: Mathematical and Physical Sciences* , 13–41 (1991).
  - [9] Michelle M Driscoll and Sidney R Nagel, “Ultrafast interference imaging of air in splashing dynamics,” *Physical review letters* **107**, 154502 (2011).
  - [10] Shreyas Mandre and Michael P Brenner, “The mechanism of a splash on a dry solid surface,” *Journal of Fluid Mechanics* **690**, 148–172 (2012).
  - [11] CD Stow and MG Hadfield, “An experimental investigation of fluid flow resulting from the impact of a water drop with an unyielding dry surface,” *Proceedings of the Royal Society of London. A. Mathematical and Physical Sciences* **373**, 419–441 (1981).
  - [12] Cacey S Stevens, “Scaling of the splash threshold for low-viscosity fluids,” *Europhysics Letters* **106**, 24001 (2014), 1403.3145.
  - [13] JE Field, JP Dear, and JE Ogren, “The effects of target compliance on liquid drop impact,” *Journal of Applied Physics* **65**, 533–540 (1989).
  - [14] Michelle M Driscoll, Cacey S Stevens, and Sidney R Nagel, “Thin film formation during splashing of viscous liquids,” *Physical Review E* **82**, 036302 (2010).
  - [15] John M Kolinski, L Mahadevan, and Shmuel M Rubinstein, “Lift-off instability during the impact of a drop on a solid surface,” *Physical review letters* **112**, 134501 (2014).
  - [16] Andrzej Latka, Arnout M. P. Boelens, Sidney R. Nagel, and Juan J. de Pablo, “Drop splashing is independent of substrate wetting,” (2016), arXiv:1607.08867.
  - [17] Antonin Marchand, Tak Shing Chan, Jacco H Snoeijer, and Bruno Andreotti, “Air entrainment by contact lines of a solid plate plunged into a viscous fluid,” *Physical review letters* **108**, 204501 (2012).
  - [18] Guillaume Riboux and José Manuel Gordillo, “Experiments of Drops Impacting a Smooth Solid Surface: A Model of the Critical Impact Speed for Drop Splashing,” *Physical Review Letters* **113**, 024507 (2014).
  - [19] A Mongruel, V Daru, F Feuillebois, and S Tabakova, “Early post-impact time dynamics of viscous drops onto a solid dry surface,” *Physics of Fluids (1994-present)* **21**, 032101 (2009).
  - [20] C.W. Hirt and B.D. Nichols, “Volume of fluid (VOF) method for the dynamics of free boundaries,” *Journal of computational physics* **39**, 201–225 (1981).
  - [21] H. Rusche, *Computational Fluid Dynamics of Dispersed Two-Phase Flows at High Phase Fractions*, Ph.D. thesis, Imperial College (2002).
  - [22] J.U. Brackbill, D.B. Kothe, and C. Zemach, “A continuum method for modeling surface tension,” *Journal of computational physics* **100**, 335–354 (1992).
  - [23] Tiezheng Qian, Xiao-Ping Wang, and Ping Sheng, “Molecular scale contact line hydrodynamics of immiscible flows,” *Physical Review E* **68**, 016306 (2003).
  - [24] J-F Gerbeau and Tony Lelievre, “Generalized Navier boundary condition and geometric conservation law for surface tension,” *Computer Methods in Applied Mechanics and Engineering* **198**, 644–656 (2009).
  - [25] A. M. P. Boelens and J. J. de Pablo, “Generalized Navier Boundary Condition for a Finite Volume Volume Of Fluid approach,” Under review (2016).
  - [26] OpenCFD Ltd, “OpenFOAM (Version 2.1.1) [Computer software],” (2011).
  - [27] G.K. Batchelor, *An Introduction to Fluid Dynamics*, Cambridge Mathematical Library (Cambridge University Press, 2000).

- [28] K Kadoya, N Matsunaga, and A Nagashima, “Viscosity and thermal conductivity of dry air in the gaseous phase,” *Journal of physical and chemical reference data* **14**, 947–970 (1985).
- [29] Irmgard Bischofberger, Kelly W Mauser, and Sidney R Nagel, “Seeing the invisible—Air vortices around a splashing drop,” *Physics of Fluids (1994-present)* **25**, 091110 (2013).
- [30] Gilou Agbaglah, Christophe Josserand, and Stéphane Zaleski, “Longitudinal instability of a liquid rim,” *Physics of Fluids (1994-present)* **25**, 022103 (2013).
- [31] John M Kolinski, Shmuel M Rubinstein, Shreyas Mandre, Michael P Brenner, David A Weitz, and L Mahadevan, “Skating on a film of air: drops impacting on a surface,” *Physical review letters* **108**, 074503 (2012).
- [32] Yuan Liu, Peng Tan, and Lei Xu, “Kelvin–Helmholtz instability in an ultrathin air film causes drop splashing on smooth surfaces,” *Proceedings of the National Academy of Sciences* **112**, 3280–3284 (2015).
- [33] SG Jennings, “The mean free path in air,” *Journal of Aerosol Science* **19**, 159–166 (1988).